

Numerical Simulation of Radio Signal from Extended Air Showers

Wei Liu^{1, 2}, Xuelei Chen^{1, 3}

¹ National Astronomical Observatories, Chinese Academy of Science, Beijing 100012, China;
xuelei@cosmology.bao.ac.cn

² University of Chinese Academy of Sciences, Beijing 100049, China;

³ Center of High Energy Physics, Peking University, Beijing 100871, China

Received ; accepted

Abstract The burst of radio emission by the extensive air shower provides a promising alternative for detecting ultra-high energy cosmic rays. We have developed an independent numerical program to simulate these radio signals. Our code is based on a microscopic treatment, with both the geosynchrotron radiation and charge excess effect included. Here we make a first presentation of our basic program and its results. The time signal for different polarizations are computed, we find that the pulses take on a bipolar pattern, the spectrum is suppressed towards the lower frequencies. We investigate how the shower at different heights in atmosphere contribute to the total signal, and examine the signal strength and distribution at sites of different elevations. We also study the signal from showers of different inclination angles and azimuth directions. In all these cases we find the charge excess effect important.

Key words: extensive air shower, geosynchrotron, charge excess effect

1 INTRODUCTION

It is well-known that the high energy cosmic rays particles could produce a large amount of secondary particles when they enter the atmosphere through cascading reactions with air molecules. These ensuing particles are called *Extensive Air Shower*(EAS). In 1965, the radio emission from these shower particles were detected for the first time (Jelley & Fruin 1965). This radio signal offers a way to detect the very high energy cosmic ray. Later, more experiments were carried out in order to further unravel the characters of this radio signal. For a review of these early activities, see Ref. Allan (1971). The radio detection technique has several advantages: it can operate round-the-clock with very little dead time, it is highly cost-effective, hence very large effective collecting area can be achieved, and it is sensitive to the atmospheric depth of the shower maximum(Huege & Pierre Auger Collaboration 2010). However, during the 1970s, as other techniques matured and were considered more reliable at the time, the research in this area dwindled.

In the last decade, with fast electronics and high-performance computers appearing, there is a revival of interest in the radio detection of cosmic rays air-showers. The “LOPES”(LOFAR PrototypE Station)(Falcke et al. 2005; Schröder et al. 2013; Apel et al. 2013) in Germany and the “CODALEMA”(COsmic ray DEtection Array with Logarithmic ElectroMagnetic Antennas)(Ardouin et al. 2009) in France experimented with the radio detection of very high energy cosmic ray particles, and a new generation of radio detectors, called the Auger Engineering Radio Array(AERA), is currently under construction in the site of Pierre Auger Observatory in south America(Huege & Pierre Auger

Collaboration 2010; Schoorlemmer & Pierre Auger Collaboration 2012; Ardouin et al. 2011). In the wake of LOPES success, cosmic ray detection appeared on the agenda of the LOw Frequency ARray (LOFAR). In Yakutsk, Russia, a radio arrays for similar purposes (Knurenko et al. 2013) have been built. A series of radio experiments (Ardouin et al. 2011; Martineau-Huynh et al. 2012), called “TREND”, have been launched by a Sino-French team in searching of ultra-high energy neutrinos, on the site of the 21cm array (21CMA) radio telescope in Xinjiang, China.

The first prediction of radio emission from the EAS was based on the idea that the extra electrons in the shower could produce coherent Cérenkov radiation at radio frequency (Askaryan 1962, 1965). However, Kahn & Lerche (1966) proposed that the geosynchrotron mechanism—the synchrotron emission of electrons moving in the geomagnetic field— as the main source of the radio emission. The radio pulses produced by the coherent geosynchrotron radiation mechanism exhibits intense polarization effect, this has been confirmed by recent experiments (Ardouin et al. 2009; Apel et al. 2010).

In recent years, a number of different programs have been developed to calculate the radio signal for a given cosmic ray shower. In one approach, the radiation is calculated by assuming a “macroscopic” model of charge and current distribution in the shower (Scholten et al. 2008; Werner & Scholten 2008). The numerical computing program *MGMR* (de Vries et al. 2010) and *EVA* (Werner et al. 2012) have been developed. In another, “microscopic” approach the radio signal is computed by sampling the shower particles, and make a coherent superposition of the synchrotron emission field of these particles. The numerical program *REAS*¹ was developed along this line (Huege & Falcke 2003, 2005a,b; Ludwig & Huege 2011). Other models have also been proposed, for example *SELFAS* (Marin & Revenu 2012; Marin 2012) and *ZHAireS* (Alvarez-Muñiz et al. 2012). The computations are fairly complicated, and there were very large differences in the predictions of these programs, with the amplitude differ by as large as a factor of 20, and also qualitatively in both the time domain (unipolar or bipolar pulse) and frequency domain (flat or suppressed low frequency spectrum). Only recently, after the charge excess effect have been included in the computation with the “endpoint formalism” (James et al. 2011), the numerical predictions of the various codes begin to converge (Huege et al. 2012).

We have developed an independent numerical program to compute the radio signals from the EAS. It is based on a microscopic model of the radio emission, and both the geosynchrotron and charge excess effect have been included. While the basic approach is to some extent similar to the *REAS* program, it is independently developed and many details of the implementation is different, hence it can furnish an independent check on the microscopic approach. In this paper, we give an introduction to our formalism and simulation program. We apply our program to study the characteristic distribution of radio pulses and their dependencies on different incident conditions, including the signal at different altitudes. It will be the basis for a program of further investigation on cosmic ray air shower radio emission.

This paper is organized as follows: in section 2 we derive the electric field from shower particles, where both geosynchrotron and radiation at the ends of particle’s trajectory (charge excess effect) are obtained and clearly distinguished. In section 3 we describe our scheme of numerical simulation. In section 4, the simulated results are presented, where both time-domain signal and frequency spectra are shown. We also study the contribution from the shower at different heights, and give the result for observers at different elevations. We also consider inclined showers and showers coming from different azimuth directions. Finally we summarize our results in section 5.

2 RADIATION FORMALISM

The canonical derivation of electric field of a moving charged particle can be found in the standard textbooks (Jackson 1998; Greiner 1998; Melrose & McPhedran 2005). The retarded potentials produced

¹ <http://www.timhuege.de/reas/>

by arbitrary-distributed sources are given by

$$\begin{aligned}\phi(\mathbf{r}, t) &= \frac{1}{4\pi\epsilon_0} \int dt' d^3\mathbf{r}' \rho(\mathbf{r}', t') \frac{\delta(t - t' - |\mathbf{r} - \mathbf{r}'|/c)}{|\mathbf{r} - \mathbf{r}'|}, \\ \mathbf{A}(\mathbf{r}, t) &= \frac{\mu_0}{4\pi} \int dt' d^3\mathbf{r}' \mathbf{j}(\mathbf{r}', t') \frac{\delta(t - t' - |\mathbf{r} - \mathbf{r}'|/c)}{|\mathbf{r} - \mathbf{r}'|},\end{aligned}\quad (1)$$

where ϵ_0 and μ_0 are respectively the permittivity and permeability in free space, and c is the speed of light in free space. Here we neglect the deviation of refractive index from its vacuum value (unity), and thus the Čerenkov effect is neglected for the present. $\delta(t - t' - |\mathbf{r} - \mathbf{r}'|/c)/|\mathbf{r} - \mathbf{r}'|$ is the Green function of corresponding wave equation (Jackson 1998), $\rho(\mathbf{r}', t')$ and $\mathbf{j}(\mathbf{r}', t')$ are respectively the charge and current density of sources, and $|\mathbf{r} - \mathbf{r}'|$ gives the distance from source position \mathbf{r}' to the observer position \mathbf{r} .

Charged particles are produced by pair creation or ionization at the shower front, and then moves with the shower, contributing to the total radiation. After moving some distance, they may lose their energy suddenly by major collisions, and left the shower. The contribution to the radiation at both ends may be important and should be taken into account. The source term of a suddenly-created and destructed moving charge can be written as

$$\begin{aligned}\rho(\mathbf{r}, t) &= e\delta^3(\mathbf{r} - \mathbf{x}(t))\theta(t - t_s)\theta(t_e - t), \\ \mathbf{j}(\mathbf{r}, t) &= ev\delta^3(\mathbf{r} - \mathbf{x}(t))\theta(t - t_s)\theta(t_e - t),\end{aligned}\quad (2)$$

where e is unit charge and $\mathbf{x}(t)$ is particle's trajectory in the geomagnetic field. $\theta(t)$ is a Heaviside step function, t_s and t_e respectively denote the starting and ending time of the motion of a charged particle (Marin & Revenu 2012). In order to integrate δ -function in Eq.(1), we introduce a new variable $u = t' + |\mathbf{r} - \mathbf{x}(t')|/c - t$, and beware of $du/dt' = 1 - \mathbf{n} \cdot \boldsymbol{\beta}$, the corresponding Lienard-Wiechert potentials can be obtained,

$$\phi = \left[\frac{e}{4\pi\epsilon_0 K R} \theta(t - t_s)\theta(t_e - t) \right]_{ret}, \quad \mathbf{A} = \left[\frac{\mu_0 e v}{4\pi K R} \theta(t - t_s)\theta(t_e - t) \right]_{ret}, \quad (3)$$

where $K = 1 - \mathbf{n} \cdot \boldsymbol{\beta}$, and $R = |\mathbf{r} - \mathbf{x}(t')|$. The quantities in the r.h.s have to be evaluated at the retarded time t' , which is determined by the retarded relationship $t = t' + R(t')/c$. The electric field are evaluated in terms of the potentials by $\mathbf{E} = -\nabla\phi - \frac{\partial\mathbf{A}}{\partial t}$, then we have

$$\begin{aligned}\mathbf{E} &= \left\{ -\nabla \left[\frac{e}{4\pi\epsilon_0 K R} \right]_{ret} - \frac{\partial}{\partial t} \left[\frac{\mu_0 e v}{4\pi K R} \right]_{ret} \right\} [\theta(t - t_s)\theta(t_e - t)]_{ret} \\ &+ \left\{ -\left[\frac{e}{4\pi\epsilon_0 K R} \right]_{ret} \nabla t' - \left[\frac{\mu_0 e v}{4\pi K R} \right]_{ret} \frac{\partial t'}{\partial t} \right\} \frac{\partial}{\partial t'} [\theta(t - t_s)\theta(t_e - t)]_{ret}.\end{aligned}\quad (4)$$

Here the first term is due to the continues motion of charge particles, while the second term accounts for the sudden creation and destruction. Noting that (Griffiths 1999),

$$\frac{\partial t}{\partial t'} = 1 - \mathbf{n} \cdot \boldsymbol{\beta}, \quad \nabla t' = -\frac{\mathbf{n}}{c \cdot (1 - \mathbf{n} \cdot \boldsymbol{\beta})}, \quad (5)$$

we have

$$\begin{aligned}\mathbf{E}(\mathbf{x}, t) &= \frac{e}{4\pi\epsilon_0} \left\{ \left[\frac{(\mathbf{n} - \boldsymbol{\beta})}{\gamma^2 K^3 R^2} \right]_{ret} + \left[\frac{\mathbf{n} \times \{(\mathbf{n} - \boldsymbol{\beta}) \times \dot{\boldsymbol{\beta}}\}}{c K^3 R} \right]_{ret} \right\} [\theta(t - t_s)\theta(t_e - t)]_{ret} \\ &+ \left[\frac{e(\mathbf{n} - \boldsymbol{\beta})}{4\pi\epsilon_0 K^2 R c} \right]_{ret} \frac{\partial}{\partial t'} [\theta(t - t_s)\theta(t_e - t)]_{ret}.\end{aligned}\quad (6)$$

In the braces, the first term is called the generalized Coulomb field and the second term is the well-known radiation field, or acceleration field. The third term indicates radiation from particle's creation and destruction. So in a neutral shower, as both positive and negative charges (electrons and positrons) move toward ground, the net contribution from third term is nearly zero. However, the electrons from air molecules are knocked out by the cosmic ray and join the shower, a real shower is negatively charged (Askaryan 1962, 1965; Alvarez-Muñiz et al. 2012). This radiation from the excess electrons have a significant contribution to the radiation, as we shall see below, and following others we shall call it the charge excess effect.

3 ALGORITHMS

3.1 Extensive Air Shower Properties

The development of the air shower can be simulated with Monte Carlo programs, such as CORSIKA(Heck et al. 1998), AIRES(Sciutto 1999) and COSMOS(Roh et al. 2013). As a first step, in this paper we apply parameterized functions to describe the distribution of shower electrons and positrons, focusing on the relation between the radio signal and shower properties, and leave the detailed modelling of the air showers to future work. Here we briefly recall the salient features of these parameterized distribution functions used in the present simulation, which were also used by Huege & Falcke (2003, 2005a).

The ‘‘Shower age’’ s is often used to mark the status of shower evolution, and a good approximation of it is

$$s(X) = \frac{3X}{X + 2X_m} , \quad (7)$$

s varies between 1 and 3. X is the atmospheric depth, which is defined as an integral of air density along the shower path,

$$X(h) = \int_h^H \frac{\rho(h)}{\cos \theta} dh , \quad (8)$$

where ρ is the atmospheric density, H the initial height of shower development and θ the zenith angle of the shower. X_m signifies the atmospheric depth where the shower reaches its maximum, viz. $s = 1$, with

$$X_m = X_0 \ln(E_p/E_c) , \quad (9)$$

where $X_0 = 36.7 \text{ g cm}^{-2}$ is the radiation length of the electron in the air, which is about 300 m at sea level and $E_c = 86 \text{ MeV}$ is the critical energy where the ionization loss of the electron equals to radiative loss. Below, as an illustration of the typical case, we shall consider a cosmic-ray proton with primary energy $E_p = 10^{17} \text{ eV}$. We model the atmosphere density $\rho(h)$ according to the US Standard Atmosphere 1977, at layer i

$$\rho(h) = \frac{b_i}{c_i} \exp\left(-\frac{h}{c_i}\right) , \quad (10)$$

where the parameters b_i and c_i for different layers are listed in table 1.

Tab. 1 Parameters for the parametrisation of the atmospheric layers(taken from (Huege & Falcke 2005a)).

Layer	Height [km]	b_i [g cm ⁻²]	c_i [cm]
1	0 – 4	1222.66	994186.38
2	4 – 10	1144.91	878153.55
3	10 – 40	1305.59	636143.04
4	40 – 100	540.18	772170.16

The profile of shower size, i.e. the total number of electromagnetic components $N(s)$ (including both electrons and positrons) at given shower age s is parameterized as (Greisen 1960):

$$N(s) = \frac{0.31}{\sqrt{X_m/X_0}} \exp \left[\frac{X_m}{X_0} \frac{2 - 3 \ln s}{3/s - 1} \right]. \quad (11)$$

And the number of particles injected per unit atmospheric depth dX is then

$$I(X) = \frac{dN(s)}{dX} + \frac{N(s)}{\lambda}, \quad (12)$$

where $\lambda \approx 40 \text{ g cm}^2$ is the mean free path of electron in the air. The atmospheric depth of single particle follows a exponential distribution $p(X) \propto \exp(-X/\lambda)$, and $\frac{N(s)}{\lambda}$ is the annihilated particles per unit radiation length.

The lateral spread of shower particles comes mainly from Coulomb scattering of electrons off the air atoms. A favourite expression for the radial distribution of electromagnetic components within the shower is the Nishimura-Kamata-Greisen(NGK) parameterization (Kamata & Nishimura 1958; Greisen 1960):

$$\varrho_{NGK}(r) = \frac{1}{r_M^2} \cdot \frac{\Gamma(4.5 - s)}{2\pi\Gamma(s)\Gamma(4.5 - 2s)} \left(\frac{r}{r_M} \right)^{s-2} \left(1 + \frac{r}{r_M} \right)^{s-4.5}, \quad (13)$$

where r_M is the Moliere radius, which characterizes transverse spreading of shower disk and a function of atmospheric depth X (Dova et al. 2003)

$$r_M = \frac{9.6}{(X - a_i)} c_i. \quad (14)$$

Showers developed at higher altitudes usually have wider lateral spread.

The thickness of the shower disk can be probed by measuring arrival time distribution. A useful fitting formula is from Agnetta et al. (1997), which contains both the curvature of the disk and the longitudinal distribution within it:

$$f(t) = At^B \exp(-Ct), \quad (15)$$

where t is the particle's arrival time at the detector relative to the shower front. Parameter A is a normalization, whereas B and C are functions of the mean arrival time $\langle t \rangle$ and corresponding standard deviation σ_t , both of which are related to radial distance to the shower center,

$$B = \left(\frac{\langle t \rangle}{\sigma_t} \right)^2 - 1, \quad C = \frac{\langle t \rangle}{\sigma_t^2},$$

$$\langle t \rangle(r), \sigma_t(r) = F + G \left(\frac{r}{r_0} \right)^H,$$

where

$$\begin{aligned} F_t &= (8.039 \pm 0.068) \text{ ns}, & F_\sigma &= (5.386 \pm 0.025) \text{ ns}, \\ G_t &= (5.508 \pm 0.095) \text{ ns}, & G_\sigma &= (5.307 \pm 0.032) \text{ ns}, \\ H_t &= 1.710 \pm 0.059, & H_\sigma &= 1.586 \pm 0.020, \end{aligned}$$

The average energy of the electrons and positrons in the air shower is about 30 MeV, where $\gamma \sim 60$ (Allan 1971). Following Huege & Falcke (2003), we parameterize the energy distribution of the cascading electrons as a broken power law, i.e.

$$p(\gamma) = \frac{\gamma}{74.2} \left(1 - e^{-(\gamma/74.2)^{-3}} \right), \quad (16)$$

where γ denotes the Lorentz factor, which varies from 5 to 1000. In this distribution, its maximum is at $\gamma = 60$.

A typical air shower is not neutral but have more electrons, whose fraction usually varies with atmospheric depth X but have a mean of 23%. Here as a first approximation, we adopt a constant value of 25%.

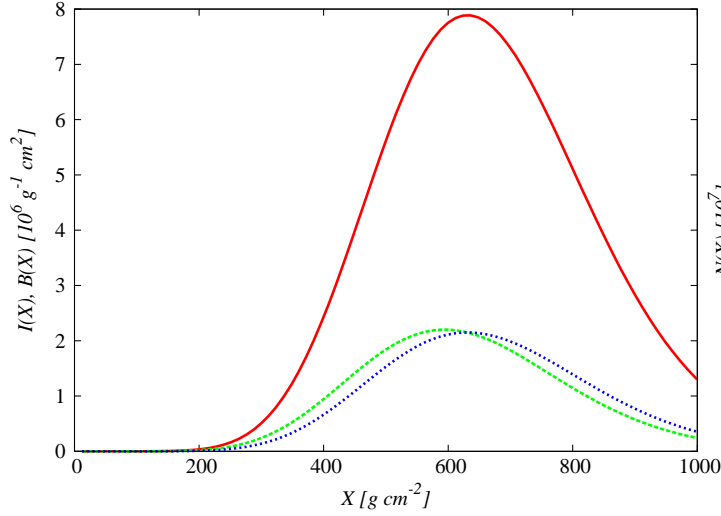


Fig. 1 $N(X)$ (red solid): the number of particles of an air shower as a function of height, $I(X)$ (green long dashed): number of injected particles per unit atmospheric depth, $B(X)$ (blue short dashed): number of annihilated particles per unit atmospheric depth.

3.2 Strategy of Numerical Simulation

We use the Monte Carlo technique to simulate the radio emission. Electrons and positrons are generated randomly according to the shower distribution functions in a frame moving with the shower center, then their positions in the ground reference frame are obtained by the coordinate transformation (see Appendix A for details). The direction of initial velocity is assumed to be along the radius of the spherical shower surface, the subsequent motion of the charged particles under the geomagnetic field is calculated according to the Lorentz formula (See Appendix B), where we have neglected the energy loss due to radiation or small angle scattering. We also use Monte Carlo to determine the free path of each particle in order to determine where the destruction take place. To take the radiation from the creation/destruction of the charged particles into account, we need to estimate the number of particle creations and destructions at each atmospheric depth, these are given by the injection rate $I(X)$ as given in Eq.(12) and destruction rate $|N(X)/\lambda|$.

In Fig.1, we plot the number of particles $N(X)$, injected particles $I(X)$ and the annihilated particles $B(X)$ at different atmospheric depths in a vertical shower(coming from the zenith). The shower begin its development high in the atmosphere, the number of particles increases as it moves downward, reaching a maximum at 631 g cm^{-2} for a 10^{17} eV cosmic ray proton, i.e. about 4000 meters high, then the number of particles begin to decrease. The injection rate $I(X)$ reaches maximum slightly earlier than the total number itself.

The time of emission and time of observation of the signal are related by a nonlinear retardation relation. Along the particle trajectory, a series of points are uniformly sampled and their contribution to the electric field at the corresponding observing time computed. We approximate the electric field to be $\bar{\mathbf{E}}(t_1) = \frac{1}{\Delta t} \int_{t_1}^{t_1+\Delta t} \mathbf{E}(t) dt$. Here Δt is the predefined time resolution, and for each segment linear approximation is made. At both endpoints of the trajectory, there are extra contributions from the creation or destruction of the particle. In Eq.(6), the third term reduces to

$$\left[\frac{e(n-\beta)}{4\pi\epsilon_0 K^2 R c} \{ \delta(t-t_s) \theta(t_e-t) - \theta(t-t_s) \delta(t_e-t) \} \right]_{ret}. \quad (17)$$

To get rid of the δ -function, we can integrate for a very short interval, $\int_{t_s-\epsilon}^{t_s+\epsilon} [\dots]_{ret} dt$, and the end point terms reduce to $\pm \left[\frac{e(\mathbf{n}-\boldsymbol{\beta})}{4\pi\epsilon_0 K R c} \right]_{ret}$.

For simplification, in our simulation we only generate electrons and positrons which acquire velocity $\sim c$, but neglected the contribution from the positively charged ions which moves with much low speed. As $K = 1 - \mathbf{n} \cdot \boldsymbol{\beta}$, and the radiation term is proportional to K^{-1} , this approximation is generally a good one. However, this omission could result in a longitudinal component of polarization when calculating the end point radiation when the electron is “created” by ionization, or “destroyed” by recombination, because it violates charge conservation at the creation and destruction point. This can be avoided by considering the contribution from the ion which are created or destroyed at the same point. The velocity of such an ion is nearly zero, and the corresponding end point radiation is $\left[\frac{e\mathbf{n}}{4\pi\epsilon_0 R c} \right]_{ret}$, with the sign just opposite to the electron being created/destroyed. So the sum of the radiation along direction of observation is

$$\begin{aligned} \pm \left[\frac{e(\mathbf{n}-\boldsymbol{\beta})}{4\pi\epsilon_0 K R c} - \frac{e\mathbf{n}}{4\pi\epsilon_0 R c} \right]_{ret} &= \pm \left[\frac{e(\mathbf{n}-\boldsymbol{\beta} - (K=1-\mathbf{n} \cdot \boldsymbol{\beta})\mathbf{n})}{4\pi\epsilon_0 K R c} \right]_{ret}, \\ &= \pm \left[\frac{e((\mathbf{n} \cdot \boldsymbol{\beta})\mathbf{n} - \boldsymbol{\beta})}{4\pi\epsilon_0 K R c} \right]_{ret}, \\ &= \pm \left[\frac{e\mathbf{n} \times (\mathbf{n} \times \boldsymbol{\beta})}{4\pi\epsilon_0 K R c} \right]_{ret}. \end{aligned} \quad (18)$$

Then the radiation from charge excess effect only contain the part whose direction of electric field is perpendicular to the direction of observation. We shall use Eq.(18) to calculate the end point radiation.

An actual shower of a 10^{17} eV proton primary have about 10^8 shower particles, but in the Monte Carlo simulation only a small fraction of these, usually a few million particles are sufficient. We estimate the electric field as

$$\hat{\mathbf{E}} = \frac{N}{n} \sum_i^n \mathbf{E}_i, \quad (19)$$

where N and n are the expected total particle number and the sampled particle number respectively. We use an adaptive control to reach the required precision in sampling: in each iteration a batch of 10^5 particles are added to the sample, and the electric field estimator at all the required locations and time grid points are updated, and compared with the value of last round. The number of location-time points where the relative change exceeds the required precision (10^{-3}) is recorded. Once such points are less than a predefined number, say 10 in 5000, the results is considered to be stable and the simulation is terminated. Our numerical program is implemented using the C programming language with the aid of the Gnu Scientific Library².

4 RESULTS

4.1 The contribution from different radiation mechanisms

To understand how the different radiation mechanisms work, we calculate the electric field signal from the pure geosynchrotron, the charge excess effect, and their sum total. First we consider a 10^{17} eV vertical shower and a 0.5 Gs magnetic field pointing due north horizontally. The shower is assumed to have an electron excess of 25%.

The electric field signal at the ground impact center of the shower axis is shown in Fig. 2, with polarizations in the East-West (EW) direction, North-South (NS) direction, and vertical direction, as well as the frequency spectrum for the signal. Under the Lorentz force from the geomagnetic field, the charged particles in the vertical shower are deflected toward east and west, as a result, we expect a

² <http://www.gnu.org/software/gsl/>

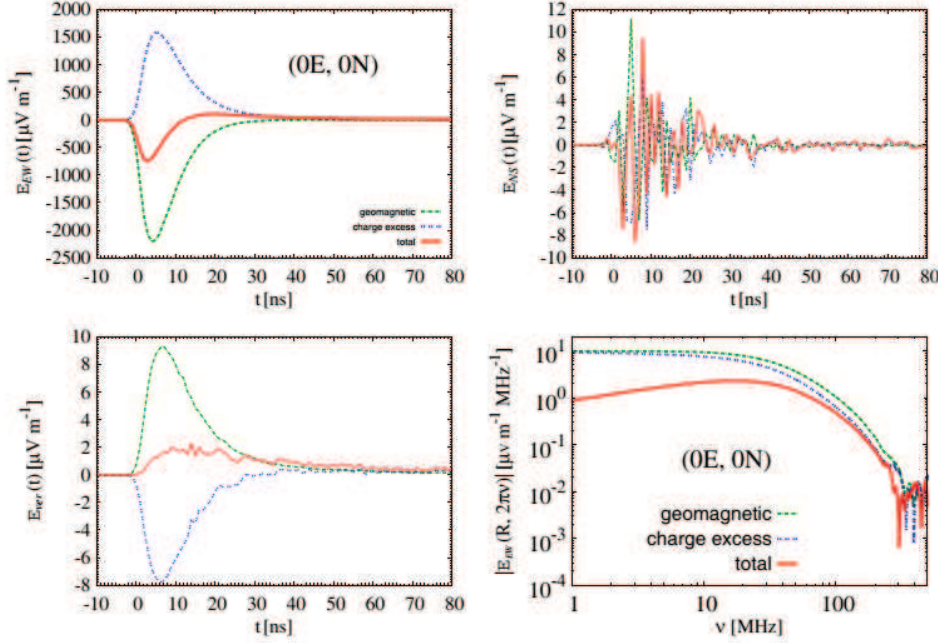


Fig. 2 The three polarization signals (upper left: EW, upper right: NS, lower left: vertical) and the frequency spectrum of the EW polarization (lower right) as observed at the shower ground center, with the pure geosynchrotron (green dash-dot curve), charge excess effect (blue dash-dot curve), and both (red solid curve).

linear polarization in the geosynchrotron radiation in the East-West (EW) direction, while the North-South (NS) polarization is expected to be small, and the vertical polarization is expected to vanish as it is along the line of sight. These expectations are confirmed in Fig. 2 where a strong pulse in the EW polarization due to the pure geosynchrotron mechanism is shown as the green dash-dotted line in the negative (west), which peaks at 8 ns, with a strength of almost $2000 \mu\text{Vm}$. The NS polarization oscillates with small amplitude, while the vertical polarization vanishes.

However, when the charge excess effect is included, we see it makes prominent and opposite contribution to the total electric field, shown as the blue dotted curve. As a result, it cancels a large part of the field generated by the geosynchrotron mechanism, especially for the primary EW polarization. The net effect, shown as the red solid curve, is a much reduced pulse, of only about $400 \mu\text{Vm}$ at its peak, and even a bipolar character where the signal at the later time is reversed in sign from the earlier one, which is different from the unipolar pattern under the pure geosynchrotron radiation. Whether the pulse is unipolar or bipolar have been debated and it was only recently resolved that the difference is due to the inclusion of the charge excess effect (Huege et al. 2012). There is also a slight vertical component at the level of $\sim 2 \times 10^{-2}$ of the total signal, probably due to the finite size of the shower disk, and also due to the asymmetry in charge.

Next we consider the signal at off-center locations. In Fig. 3, we plot the signals at a site 100m due north of the ground center (top 4 panels), and a site 100m west of the ground center (bottom 4 panels). Again, many of the basic features are similar to the case in the ground center, with the EW polarization still the dominant one, though the amplitude is smaller than at the ground center. In the off-center case, the NS polarization may be present, but interestingly, in the 100m north case, both the

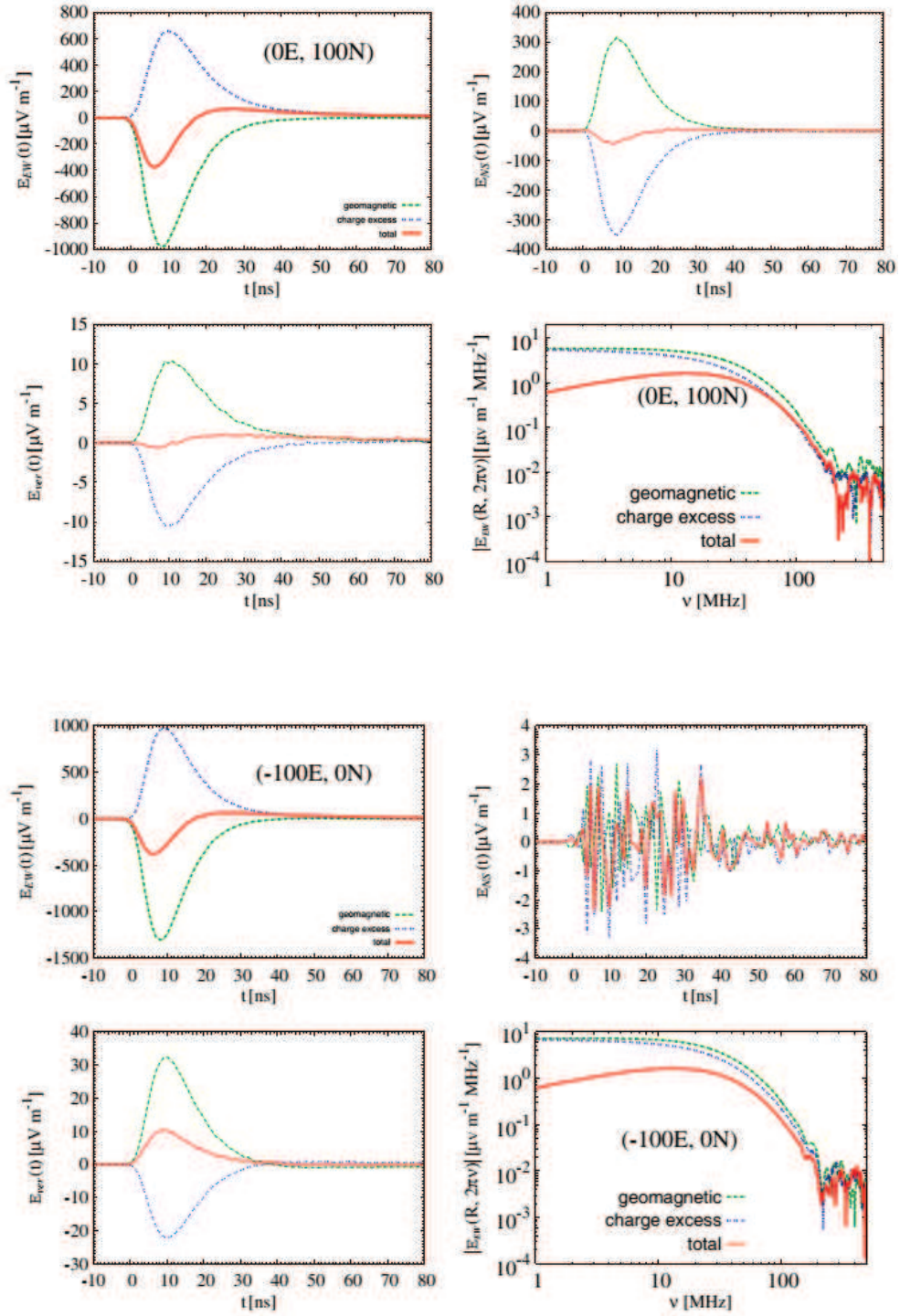


Fig. 3 The same as Fig. 2, except at off-center site. Top 4 panels: 100m north of the shower ground center, Bottom 4 panels: 100m west of the shower ground center.

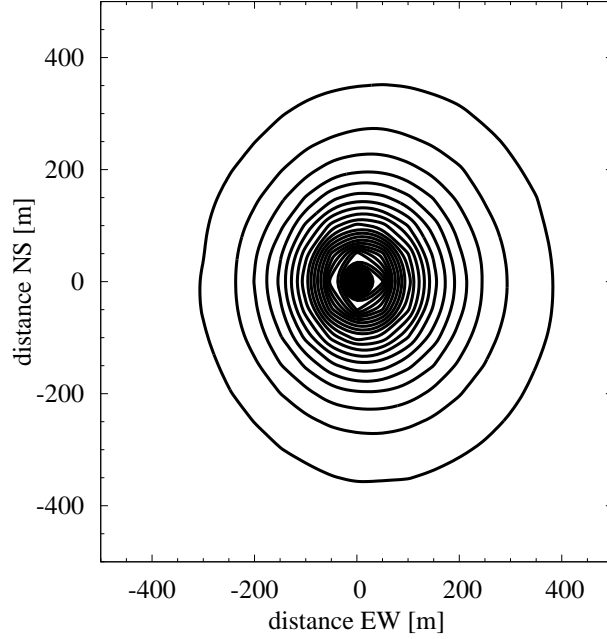


Fig. 4 The contour of electric field maximum of EW polarization from a vertical shower. The contour levels are $25\mu Vm^{-1}$ apart.

the pure synchrotron and the charge excess effect alone could produce relatively large peak, but they nearly cancel each other and the net effect is a relatively small peak.

The whole pattern of the shower signal is shown in Fig. 4. The signal is highly beamed, and we can see there is a slight asymmetry in the EW direction. The shower is nearly vertical, but the Lorentz force deflects motion of particles, and there is a net charge excess in the shower, in the end it produced the pattern as shown in Fig. 4.

4.2 Frequency Spectra Fitting

In Fig. 2 and Fig. 3, we have also plotted the frequency spectrum of the radiation for different mechanisms (bottom right panels in each of the four-plot combination). The major component of the radio emission lies in the frequency range of about tens of MHz, in agreement with observations.

At the high frequency end, we see from these figures that for both the geosynchrotron and the charge excess effect, the spectra fall off exponentially above ~ 100 MHz, though the charge excess radiation decays slightly earlier than the geosynchrotron radiation. As a result, the total spectra also falls off. This spectral drop off is due to the loss of coherence, because at such high frequencies the wave length is far less than the thickness of the shower, and the contribution to the field strength from different part of the shower no longer simply adds up. As a result, the radiation is insignificant at such high frequencies.

At the low frequency end, we can see from these figures that for both the geosynchrotron and charge excess effect the spectra is nearly flat. However, as the two are in opposite direction, they cancel each other, and the total signal have a slowly decreasing spectrum at the lower frequencies. This cut off at the lower frequency due to the cancellation effect has been noted in the recent literature (Werner & Scholten 2008; Ludwig & Huege 2011; Marin & Revenu 2012; Alvarez-Muñiz et al. 2012).

Experimentally, analyses of a few strong events by the CODALEMA (Ardouin et al. 2006) and LOPES (Nigl et al. 2008; Haungs et al. 2009) experiment show that in the range of 30 – 70 MHz,

the frequency spectrum can be well fitted with a single power-law $\epsilon_\nu = K \cdot \nu^{-\alpha}$ with spectral index $\alpha = -1 \pm 0.2$, or alternatively by an exponential function $\epsilon_\nu = K \cdot \exp(\nu/\text{MHz}/\beta)$, where β spans from -0.021 to -0.013 . This is slightly steeper than the slope predicted by the pure geosynchrotron. In these experiments, they found no significant dependence of the spectral slope on the distance to the shower axis, the zenith angle or the azimuth angle.

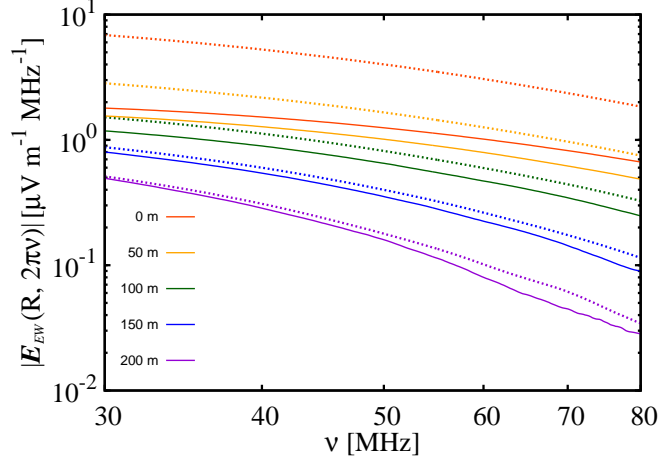


Fig. 5 The frequency spectra at different radial distances to the east of shower ground center. The distances are respectively 0 meter, 50 meters, 100 meters, 150 meters, 200 meters. Short dash lines: only geosynchrotron radiation; Solid lines: with both geosynchrotron and charge excess effect.

Tab. 2 The fitted parameters of the frequency spectrum at different radial distances along the east and west direction. We fit with a single power law $\epsilon_\nu = K \cdot \nu^{-\alpha}$ between 40 – 70 MHz.

Distance	Orientation	E_0 (pure)	α (pure)	E_0 (both)	α (both)
0 m	center	1114.72	1.442	96.37	1.114
50 m	east	1114.72	1.442	161.56	1.301
	west	1403.90	1.565	132.16	1.268
100 m	east	573.62	1.680	520.54	1.714
	west	2836.44	1.893	410.51	1.681
150 m	east	2425.63	2.233	3846.32	2.383
	west	10454.02	2.405	3152.25	2.375
200 m	east	17889.64	2.952	110199.9	3.453
	west	50671.17	3.012	93022.37	3.464

In Fig. 5 we plot the simulated spectra at different distances from the ground center for a vertical shower. Short dash lines are the spectra for the pure geosynchrotron, while solid lines are those including charge excess effect. The distances to shower impact center are respectively 0 meter, 50 meters, 100 meters, 150 meters, 200 meters. We also fit these spectra with a single power law $\epsilon_\nu = E_0 \cdot \nu^{-\alpha}$ in the range of 40 – 70 MHz, the fitting values of E_0 and α are reproduced in table 2, for distances measured to both the east and the west of the ground center, as there is a slight asymmetry as we noted

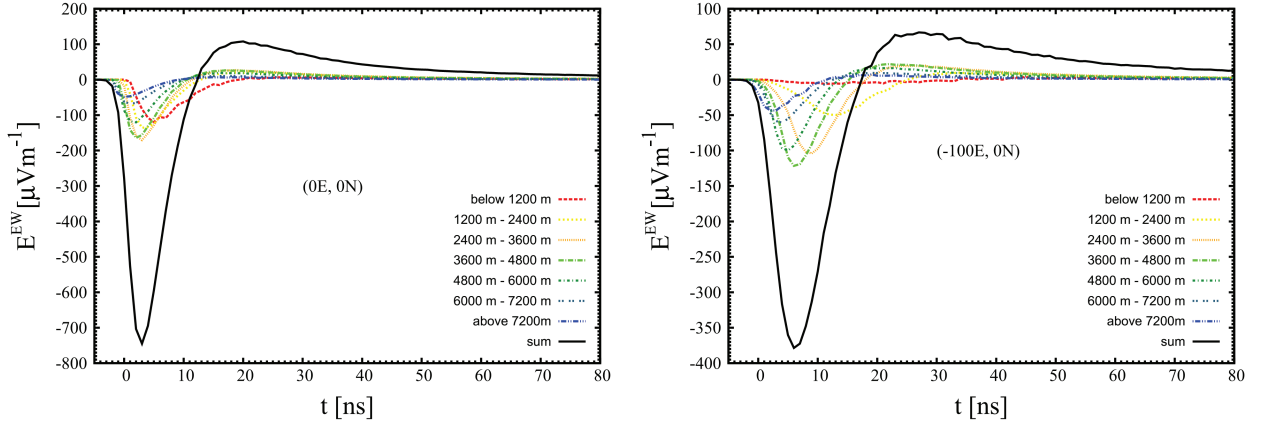


Fig. 6 Left: Contribution from layers at different heights at the shower ground center. Right: Contribution from layers at different heights at 100m west from the shower ground center.

before. It is apparent that within 150 meters, the single power law is a good fit to the spectrum. With the radial distances increasing, the slope becomes steeper. Near the center (within 50 m) part, the slope of the spectrum including both geosynchrotron and charge excess effect is -1 ± 0.2 , consistent with the experiment result. On the other hand, for the pure geosynchrotron radiation the slope α conflicts with the experimental results, and the difference is larger than the margin of error. This shows that the inclusion of the charge excess effect is very important.

However, far away from the center, both the pure geosynchrotron model and the model with charge excess effect predict steepening of the spectra, while observations so far have not found such change. Part of this may be due to experimental error, because far from the shower ground center, the signal strength falls off exponentially, and the resulting measurement error is large. Another possibility is, the Čerenkov radiation may have visible effect at intermediate distances (de Vries et al. 2012), and may modify the corresponding frequency spectrum.

4.3 Contribution from different Elevations

We now study how the shower at different heights contribute to the total signal at the ground level. If the shower is point-like, there would be a one-to-one relation between the emission time and arrival time for the radio pulse, with the radiation emitted earlier arrive earlier, and the envelope of the signal would clearly reflect that of the shower at different heights (Alvarez-Muñiz et al. 2012). However, the real case is more complicated due to the spatial extent of the shower disk, for at any given time the signal received on a location in the ground (altitude 0) is a superposition of emissions from different parts of the shower at different times. The problem of contribution from different heights in the case of pure geosynchrotron was investigated by Huege et al. (2007), here we consider the case with charge excess effect.

We compute the radio signal contribution from different height layers, the results are shown in Fig. 6. For illustration, we have chosen two observing sites, one at the shower ground center and one at 100m-west off center.

Starting from the ground, we divide the whole atmosphere into 7 segments, each segment have an intervals of 1200 m, except for the highest one, where we combine all contributions from above 7200 m. We plot the contribution of each layer as well as the total signal. A general impression is, each layer can contribute both to the first, strong (negative) peak as well as the second, weak (positive) peak, though the higher layers contribute more to the first while the lower ones contribute more to the second. The

3600 – 4800 m and 2400 – 3600m layers contribute the largest signal, these two are also the layers which contain the maximum number of particles. The contributions from the higher elevations are smaller but still significant. The contribution of the lower layers (0 – 1200m and 1200 – 2400m) are also sizeable, they are closer to the observer, but the number of particles have decreased. In particular, the contribution of 0 – 1200m is sizeable in the ground center, but away from ground center it is much less, due to the relativistic beaming.

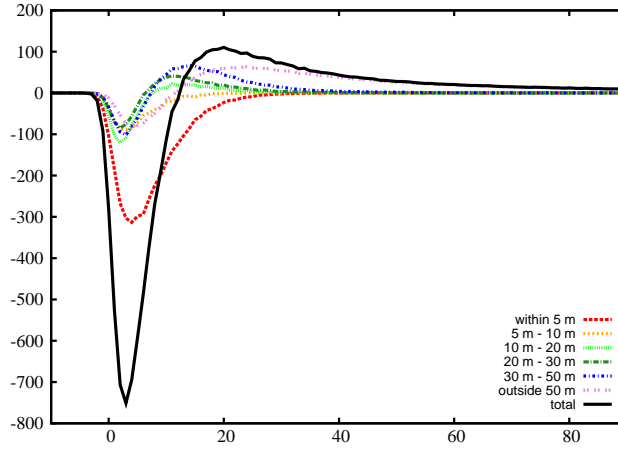


Fig. 7 Contributions at different lateral distances to shower axis. The intervals are within 5 meters, 5 – 10 meters, 10 – 20 meters, 20 – 30 meters, 30 – 50 meters, and beyond 50 meters.

We further compute the contribution from different lateral distances, see Fig. 7. The observing site is chosen to be the shower center. We make concentric rings around the shower axis, first ring within 5m, then 5 – 10m, 10 – 20 m, 20 – 30 m, 30 – 50 m, and beyond 50 meters, and estimate the contribution from each. The main contribution comes from the distance within 50 meters, especially within 5 m. This is because most of the shower particles are located in the inner rings near the center of the shower, as the horizontal motion caused by geomagnetic field is small compared with shower velocity.

4.4 Signals for observing at different elevations

The particle based cosmic ray detectors are often placed at sites of high altitudes, because the shower maximum is high in the atmosphere, and radio detectors may also be located on the same sites, so it is important to consider the altitude effect on the radio signal. As we get closer to the shower maximum, we may receive stronger emission from this stage. On the other hand, at the higher elevation, the signals from the later stage of the shower is missed.

Fig. 8 shows how the peak field strength of the radio pulse varies with observation site elevation for a vertical shower at several offset differences from the ground center. In all cases the variation is apparent but not very rapid. In the case of shower ground center, the signal strength raises gradually at the beginning and reaches its maximum value at around 4000 meters high, where the shower develops to its maximum for a 10^{17} eV cosmic ray. At still higher altitude, the signal begin to attenuate. In the off center cases, the peak strength drops off with increasing altitude, and for the three off-center distances we computed, the variations have similar dependencies on height. This result show that if the radio detector array is primarily designed primarily to detect the signal in the center area, then there is a little advantage to choose a site of high altitude, though it is far less significant as in the case of particle detectors. On the other hand, if the radio array is sensitive enough to detect showers outside the center area, then perhaps there is not much advantage to place the detector on high altitudes.

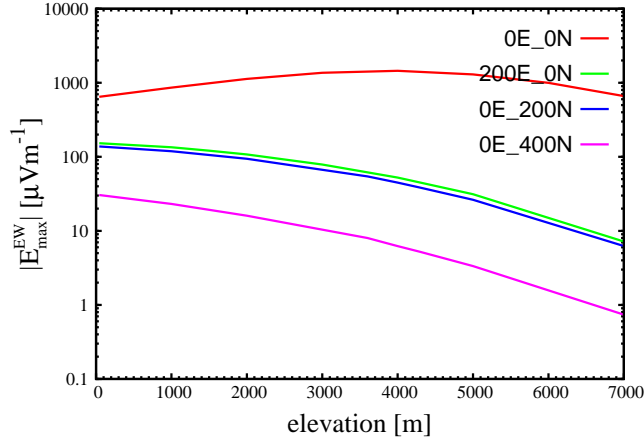


Fig. 8 Elevation dependence of the radio signal. Signals at four locations (ground center, 200m due East to the center, 200m due North to the center, 400m due North to the center) are plotted as a function of ground altitude.

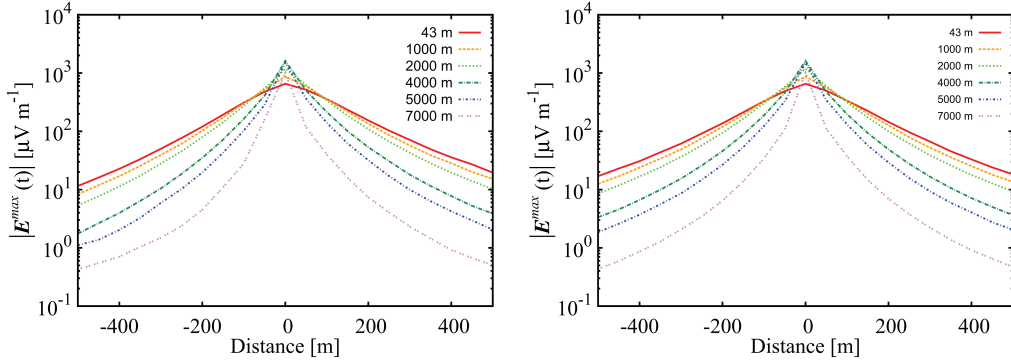


Fig. 9 The peak field strength of the pulse as a function of off-center distance in the EW (top) and NS (bottom) directions.

In Fig. 9 we plot the lateral distribution of the radio signal at different elevations for a vertical air shower. There is a slight asymmetry of lateral distribution along the EW direction about shower axis, where the signal in the east is stronger. This is caused by the excess of electrons in the shower, but this does not affect the NS distribution. Close to the shower axis, the peak electric field strength raises with the increase of elevation until about 4000m, where the shower reaches the maximum for a 10^{17} eV cosmic ray primary. Away from the shower axis, the strengths always decreases with the height. The turning point between the *center* and *off-center* is at around 50 meters. The radial dependence of electric field signal is usually parametrized by an exponential function

$$\varepsilon(r) = \varepsilon_{100} \exp(-(r - 100\text{m})/R_0), \quad (20)$$

where ε_{100} is the amplitude at 100 m and scale parameter R_0 is usually about 100 to 250 meters, except for some events which has a very large R_0 (Haungs et al. 2009; Apel et al. 2010). We use Eq.(20) to fit

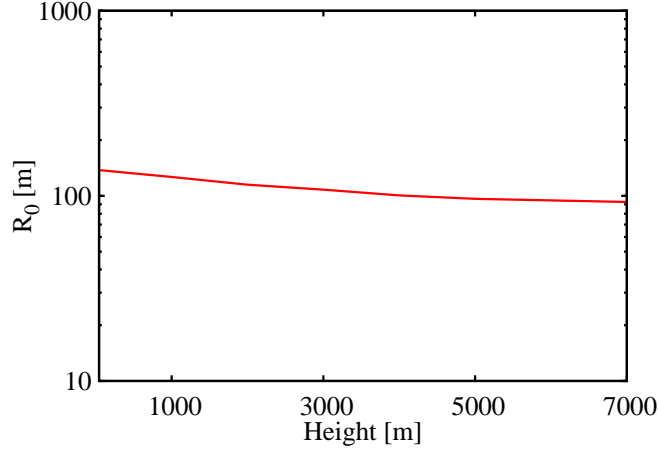


Fig. 10 Elevation dependence of the scale R_0 .

the lateral distribution in the range of 200 – 500m at different elevations, and show the variations of R_0 with heights in fig. 10. We can see that R_0 do not change significantly with height.

4.5 Inclined showers: zenith angle and azimuth angle dependence

So far we have been considering only vertical showers, but inclined showers are of course more common. The inclined showers share some general characters with the vertical ones, now we will investigate how the shower behaviour changes as the inclination angle varies. The zenith dependence of radial distribution is shown in Fig. 11. At the shower center, the field strength decreases with zenith angle, the vertical shower have the largest peak strength. However, the inclined showers have broader distribution, so some distance away from the center they may actually have greater field strength.

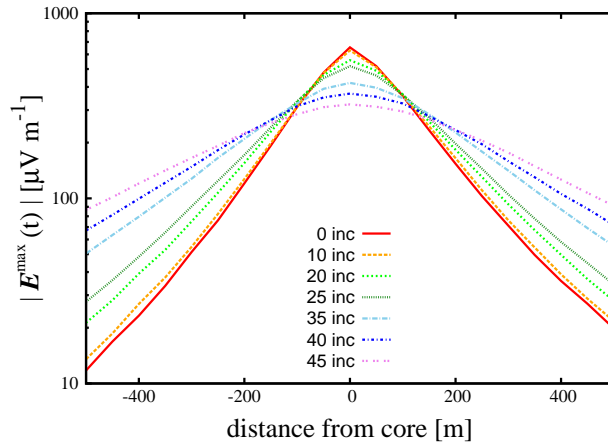


Fig. 11 The radial distribution of the magnitude of radio signal under different zenith angles.

In Fig. 12, we show the contours of radio emission field strength with different zenith angles, where the shower axis is assumed to be inclined from the east direction with different angles. Such spatial

distribution could be detected with a phalanx of radio signal receivers, and we show the distribution for the total strength as well as the polarized electric field along the EW, NS and vertical directions.

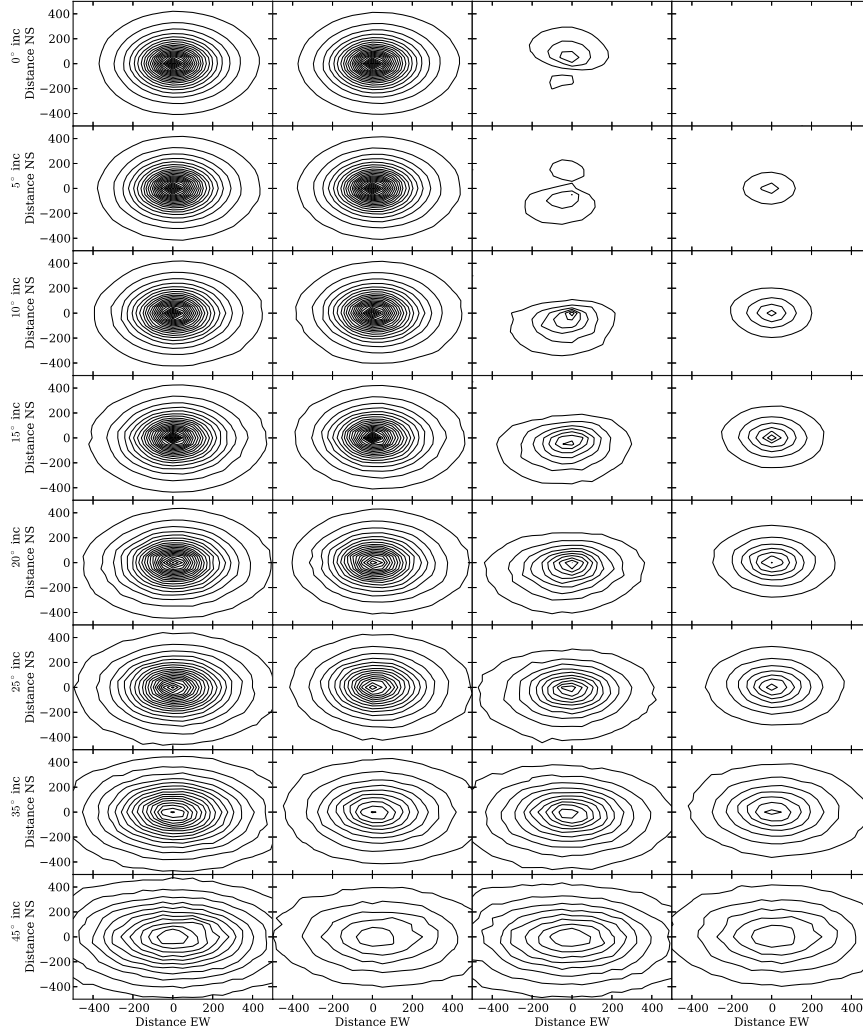


Fig. 12 The contours of unfiltered radio emission under different zenith angles. Columns from left to right: total field strength, the EW polarization, the NS polarization, and the vertical polarization. Lines from top to bottom are with zenith angle of 0° , 5° , 10° , 15° , 20° , 25° , 35° , 45° respectively. Contour levels are $25\mu\text{Vm}^{-1}$ apart.

For a vertical shower (zenith angle 0°), the total field strength and the dominant EW polarization components have a distribution of concentric ellipses. The NS and vertical polarizations, on the other hand, exhibit asymmetric bivalve structures in this case. This asymmetry is due to the effect of magnetic field, which breaks the otherwise totally symmetric arrangement in the vertical shower.

With increasing zenith angles, the total field strength and the dominant EW polarization decreases slightly and their contour ellipses become more prolate along the EW direction, and the axis of the contour ellipses become longer. At the same time, the bivalve structures in the NS and vertical components change to concentric ellipses and now these components have greater magnitudes than the vertical case. their magnitudes gradually grows. These changes are consistent with our expectation for a slanted grant cross section with respect to the shower axis.

The contour maps from different incident azimuth directions in the case of pure geosynchrotron were studied in [Huege & Falcke \(2005b\)](#). Besides elongation of field strength pattern, they found total field strength pattern rotates with the azimuth angle. The measurements of the individual polarization components can be used to verify directly the geosynchrotron origin of the signal in radio emission.

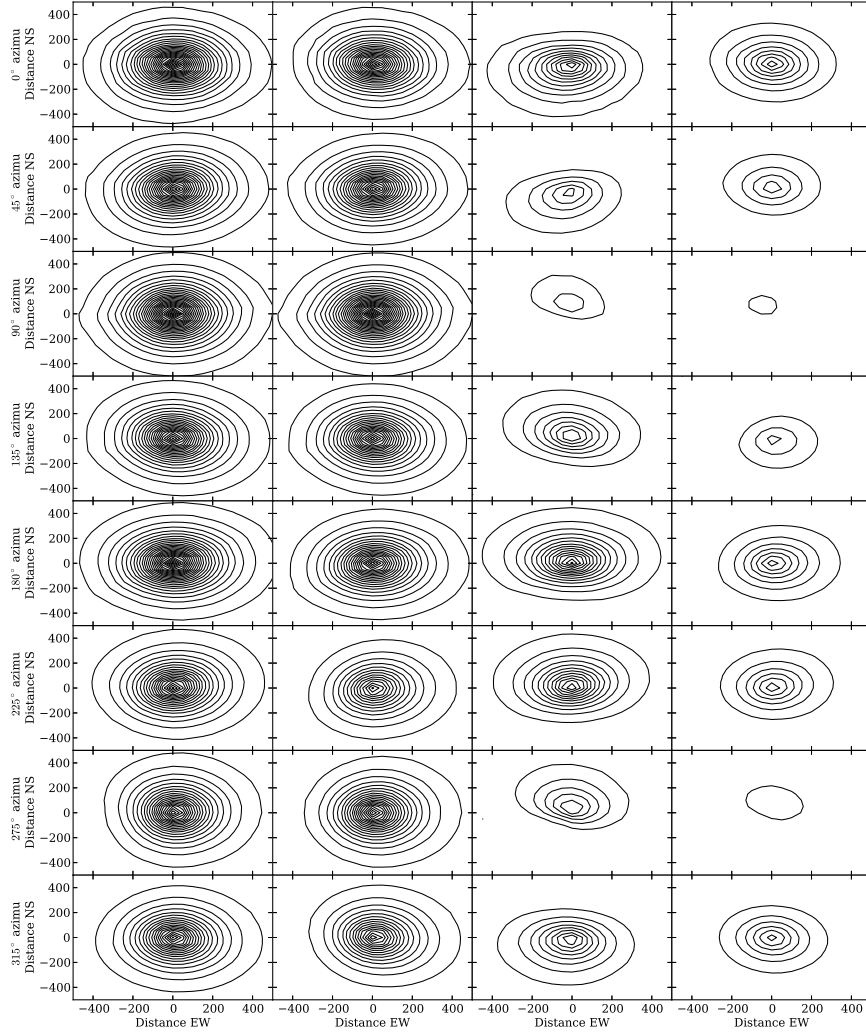


Fig. 13 The contours of unfiltered radio emission for a 20° -inclined shower coming from different incident azimuthal directions. Columns from left to right are respectively the total field strength, the EW polarization, the NS polarization, and the vertical polarization. Lines from top to bottom are with azimuth angle of 0° , 45° , 90° , 135° , 180° , 225° , 270° , 315° respectively. Contour levels are $25\mu\text{Vm}^{-1}$ apart.

With the inclusion of the charge excess and creation/destruction effect, the situations become more complicated. As shown in Fig. 13, the contours of the total field strength show concentric ellipses, while there are some slight changes in the orientation of these ellipses, it is not very obvious. This is not surprising, for with both the geosynchrotron and creation/destruction emission at work, the geometric relation is more complicated. Again, the NS and vertical polarizations show more irregularity, in some cases with bivalve pattern.

5 CONCLUSION

In this paper, we describe our new Monte Carlo simulation of the radio signal emitted by cosmic ray extensive air showers. Our basic approach is similar to *REAS2*, using Monte Carlo to generate a sample of particles and calculate the field produced by them, but we included the charge excess effects in addition to the geosynchrotron radiation. We use step functions in the retard potentials to express the creation and destruction of particles. At low frequency, the radiation field can be derived classically. The algorithm of our numerical program is presented which has passed preliminary checks and gives results which are consistent with the ones obtained by others.

We find that when the charge excess effect is included, the radio signal is significantly modified: the magnitude of the signal is substantially reduced, and in the time domain the pulse EW polarization exhibits a bipolar pattern. This is the most important distinction to the previous pure geosynchrotron radiation. The charge excess effect on the frequency spectrum is also considered. The geosynchrotron and charge excess effect, when computed individually, have similar spectra which drops at $\sim 100\text{MHz}$ due to the loss of coherence. At low frequencies both have flat spectrum, but when added the two tends to cancel each other and the spectrum drops also at the lower end. These findings are in good agreement with recent results reported in the literature (Huege et al. 2012). We also computed the spectra at different locations. Near the center, the charge excess effect amends the steep spectrum predicted by the pure geosynchrotron mechanism, and the combined spectrum is in agreement with the observation. Off the center, the theoretical spectrum is steeper than the observation. This may be due to experimental error, or another kind of radiation, such as the Cerenkov radiation.

We further apply our program to study the features of the signals. For a vertical shower and near the shower axis, we find that the signal at any time comes from a wide span of different heights, and indeed the layers from different heights could all give sizeable contributions to the total signal, though the shower maximum contributed most. Far off center, the contribution from the shower maximum dominates, while near the center, the lower altitude layers could also contribute a large share.

We study the elevation dependence of the signal. At the shower center, as the altitude raises, the peak magnitude increases slightly, then drops off if the altitude reaches beyond that of the shower maximum. Off center, it always decreases with increasing altitude. This means that there is slight advantage to place the radio array detector at sites of high altitude, if the array is designed to detect the radio signal at center. On the other hand, if the array is sufficiently sensitive to be able to detect the radio emission at large off-center distance, then there is not much advantage to place it at high altitudes. Indeed, even in the former case, the advantage is far less obvious than the particle-based detector. We use an exponential function to fit the radial distributions and find R_0 is about 100 meters, which is consistent with experimental results.

We then consider the inclined showers with different zenith and azimuth angles, and computed spatial distribution of the signal. We find that the contour lines of signal strength are basically concentric ellipses, but due to the asymmetry of charges, there is an azimuthal asymmetry in the EW polarization even for a vertically-downward air shower. The total field strength and the dominant EW polarization decrease gradually as the zenith angle increases, and the ellipses are elongated. However, the addition of the charge excess effect obscured the signature of the geosynchrotron effect, the azimuthal dependence of the total field strength is not apparent. In the NS polarization, the shape is also changed from pintongs to bivalve pattern. Our program could be a useful tool for incoming radio detection study.

This paper presents a very basic model of cosmic ray air shower radio emission, and some similar results have been obtained previously. Nevertheless, it is useful to verify these results with an indepen-

dent computation as we did, and to examine how the signal varies with elevation, shower inclination and azimuth angle, etc. Moreover, it is a first step toward an independent, comprehensive numerical study of the air shower radio emission problem. We are working to improve our model by incorporating more physics effects and implement more realistic models. We plan to use a shower model generated by a modern Monte Carlo code (e.g. CORSIKA). The effect from the variation of atmospheric refractive index and the corresponding Čerenkov radiation will also be investigated in our subsequent works. We can then investigate showers of different energy and composition, and then it will be useful to the radio detection experiments.

ACKNOWLEDGEMENT

We would like to thank Tim Huege for providing us the Reas2.59 code for comparison. This work is supported by the Ministry of Science and Technology 863 project 2012AA121701, by the Chinese Academy of Science Strategic Priority Research Program “The Emergence of Cosmological Structures” of the Chinese Academy of Sciences, Grant No. XDB09000000, and the NSFC grant 11373030.

Appendix A: COORDINATE TRANSFORMATION

In this part, the position and velocity of a charged particle in the Earth reference frame are related to its relative position in the shower disk. In an incident shower with zenith angle Θ , the center of the disk plane is set to be the origin O' of the (moving) shower coordinates. The X' axis is in the plane of the incidence, pointing horizontally outwards, and Y' axis is in the disk plane and normal to the X' axis with right hand side direction. The Z' points upward (see the right panel of Fig. A.1). The relative position of the particle P can be written as

$$\mathbf{R}'_r = \begin{cases} r \cos \varphi \cos \Theta , \\ r \sin \varphi , \\ -r \cos \varphi \sin \Theta , \end{cases} \quad (\text{A.1})$$

where r is the distance from the origin O' and φ is the azimuthal angle around the disk plane which rotates counterclockwise from lower part of shower disk.

The coordinate \mathbf{R}_r of P can be transformed from the $X'O'Y'$ to the system XOY ,

$$x = x' \cos \Phi - y' \sin \Phi , \quad (\text{A.2})$$

$$y = y' \cos \Phi + x' \sin \Phi . \quad (\text{A.3})$$

Here in the XOY plane, the X and Y axis respectively point to the east and north(see left figure of A.1). Φ is the azimuthal angle in the system XOY .

The position of O' in the XYZ system, where the impact center O is set to be the origin, is given by

$$\mathbf{R}_{O'} = \mathbf{R}_{\text{sf}} \times (R_{\text{sf}} + d)/R_{\text{sf}} , \quad (\text{A.4})$$

where \mathbf{R}_{sf} is the position of center of shower front in the XYZ system, which is equal to $\mathbf{R}'_{\text{sf}} - H \hat{e}_z$, if the impact center is H meters above the sea level. Position \mathbf{R}'_{sf} could be evaluated according to the relation between height and atmospheric depth X which is produced by a random number generator in the Monte Carlo code(see subsection 3.1), d is the distance from the shower front. The position in system XYZ can be further obtained from the vector relationship

$$\mathbf{R}_p = \mathbf{R}_{O'} + \mathbf{R}_r . \quad (\text{A.5})$$

Finally the absolute position is

$$\mathbf{R}_p = H \hat{e}_z . \quad (\text{A.6})$$

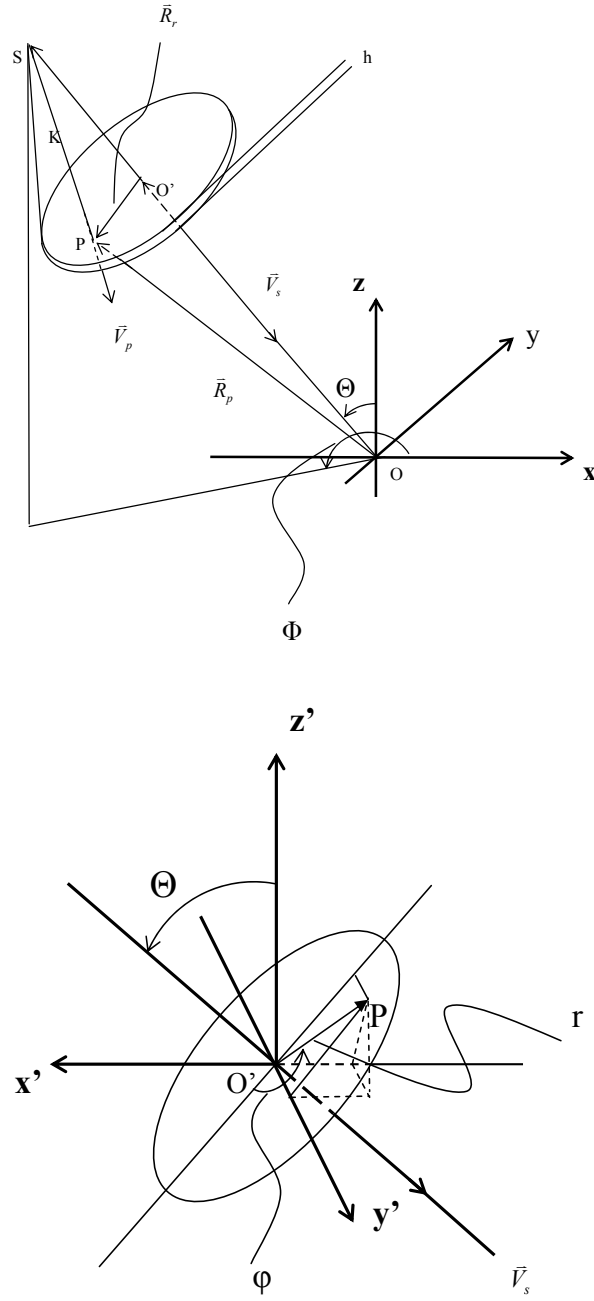


Fig. A.1 Top: a sketch of shower disk in Earth's coordinate system XYZ , with X and Y respectively pointing to the east and north. Down: shower disk in local system $X'O'Y'$.

Secondary particles are assumed to be distributed within the spherical shell, with radius K equal to 2300 m. Therefore their initial velocity direction is assumed to be radial, i.e.

$$\hat{\mathbf{V}}_p = \frac{\mathbf{R}_p - \mathbf{R}_s}{|\mathbf{R}_p - \mathbf{R}_s|}, \quad (\text{A.7})$$

where

$$\mathbf{R}_s = \mathbf{R}_{O'} \times (R_{O'} + K)/R_{O'}. \quad (\text{A.8})$$

Appendix B: THE MOTION OF A CHARGED PARTICLE IN MAGNETIC FIELD

The motion of a single charged particle in a static uniform magnetic field is determined by the Lorentz equation

$$\gamma m \frac{d\mathbf{V}}{dt} = -q\mathbf{V} \times \mathbf{B}, \quad (\text{B.1})$$

where γ is the Lorentz factor. Cross product \mathbf{B} on both sides, differentiating it, use Eq.(B.1) and the vector identify $\mathbf{B} \times (\mathbf{V} \times \mathbf{B}) = \mathbf{V}B^2 - \mathbf{B}(\mathbf{V} \cdot \mathbf{B})$, we get a second-order differential vector equation

$$\frac{d^2\mathbf{V}}{dt^2} + \left(\frac{q\mathbf{B}}{\gamma m}\right)^2 \mathbf{V} - \left(\frac{q}{\gamma m}\right)^2 \mathbf{B}(\mathbf{V} \cdot \mathbf{B}) = 0. \quad (\text{B.2})$$

By dot-producting \mathbf{B} in both sides of the Lorentz equation,

$$\frac{d(\mathbf{V} \cdot \mathbf{B})}{dt} = 0, \quad (\text{B.3})$$

i.e. $\mathbf{V} \cdot \mathbf{B} = \text{const}$, so the solution of Eq.(B.2) is

$$\mathbf{V}(t) = \mathbf{a}_1 \cos \omega_B t + \mathbf{b}_1 \sin \omega_B t + \frac{\mathbf{B}(\mathbf{V}_0 \cdot \mathbf{B})}{B^2}, \quad (\text{B.4})$$

where $\omega_B^2 = (q\mathbf{B}/\gamma m)^2$ is the gyration frequency of the circular motion, and \mathbf{V}_0 is the initial velocity. The constants \mathbf{a}_1 and \mathbf{b}_1 can be determined from the initial conditions,

$$\mathbf{a}_1 = \mathbf{V}_0 - \frac{\mathbf{B}(\mathbf{V}_0 \cdot \mathbf{B})}{B^2}, \quad \mathbf{b}_1 = \frac{q(\mathbf{a}_1 \times \mathbf{B})}{\gamma m \omega_B}. \quad (\text{B.5})$$

The trajectory of the particle can then be integrated, which is given by

$$\mathbf{X}(t) = \frac{\mathbf{a}_1}{\omega_B} \sin \omega_B t - \frac{\mathbf{b}_1}{\omega_B} (\cos \omega_B t - 1) + \frac{\mathbf{B}(\mathbf{V}_0 \cdot \mathbf{B})}{B^2} t + \mathbf{X}_0, \quad (\text{B.6})$$

where \mathbf{X}_0 is the initial position.

References

- Agnetta, G., Ambrosio, M., Aramo, C., et al. 1997, *Astroparticle Physics*, 6, 301 [5](#)
Allan, H. R. 1971, *Prog. in Element. Part. and Cos. Ray Phys.*, 10, 171 [1](#), [5](#)
Alvarez-Muñiz, J., Carvalho, W. R., & Zas, E. 2012, *Astroparticle Physics*, 35, 325 [2](#), [4](#), [10](#), [12](#)
Apel, W. D., Arteaga, J. C., Asch, T., et al. 2010, *Astroparticle Physics*, 32, 294 [2](#), [14](#)
Apel, W. D., Arteaga, J. C., Bähren, L., et al. 2013, *ArXiv e-prints* [1](#)
Ardouin, D., Belletoile, A., Berat, C., et al. 2009, *Astroparticle Physics*, 31, 192 [1](#), [2](#)
Ardouin, D., Belletoile, A., Charrier, D., et al. 2006, *Astroparticle Physics*, 26, 341 [10](#)
Ardouin, D., Cârloganu, C., Charrier, D., et al. 2011, *Astroparticle Physics*, 34, 717 [2](#)
Askaryan, G. A. 1962, *Journal of the Physical Society of Japan Supplement*, 17, C257 [2](#), [4](#)
Askaryan, G. A. 1965, *Soviet Journal of Experimental and Theoretical Physics*, 21, 658 [2](#), [4](#)

- de Vries, K. D., Scholten, O., & Werner, K. 2012, *Nuclear Instruments and Methods in Physics Research A*, 662, 175 [12](#)
- de Vries, K. D., van den Berg, A. M., Scholten, O., & Werner, K. 2010, *Astroparticle Physics*, 34, 267 [2](#)
- Dova, M. T., Epele, L. N., & Mariazzi, A. G. 2003, *Astroparticle Physics*, 18, 351 [5](#)
- Falcke, H., Apel, W. D., Badea, A. F., et al. 2005, *Nature*, 435, 313 [1](#)
- Greiner, W. 1998, *Classical Electrodynamics*, Classical Theoretical Physics Series (Springer Verlag) [2](#)
- Greisen, K. 1960, *Annual Review of Nuclear and Particle Science*, 10, 63 [5](#)
- Griffiths, D. J. 1999, *Introduction to Electrodynamics* (3rd Edition) (Benjamin Cummings), 3rd edn. [3](#)
- Haungs, A., Apel, W. D., Arteaga, J. C., et al. 2009, *Nuclear Physics B Proceedings Supplements*, 196, 297 [10](#), [14](#)
- Heck, D., Knapp, J., Capdevielle, J. N., Schatz, G., & Thouw, T. 1998, CORSIKA: a Monte Carlo code to simulate extensive air showers. [4](#)
- Huege, T., & Falcke, H. 2003, *A&A*, 412, 19 [2](#), [4](#), [5](#)
- Huege, T., & Falcke, H. 2005a, *A&A*, 430, 779 [2](#), [4](#)
- Huege, T., & Falcke, H. 2005b, *Astroparticle Physics*, 24, 116 [2](#), [17](#)
- Huege, T., Ludwig, M., Scholten, O., & de Vries, K. D. 2012, *Nuclear Instruments and Methods in Physics Research A*, 662, 179 [2](#), [8](#), [19](#)
- Huege, T., & Pierre Auger Collaboration 2010, *Nuclear Instruments and Methods in Physics Research A*, 617, 484 [1](#)
- Huege, T., Ulrich, R., & Engel, R. 2007, *Astroparticle Physics*, 27, 392 [12](#)
- Jackson, J. D. 1998, *Classical Electrodynamics*, 3rd Edition [2](#), [3](#)
- James, C. W., Falcke, H., Huege, T., & Ludwig, M. 2011, *Phys. Rev. E*, 84, 056602 [2](#)
- Jelley, J. V., & Fruin, J. H. 1965, *Nature*, 205, 327 [1](#)
- Kahn, F. D., & Lerche, I. 1966, *Royal Society of London Proceedings Series A*, 289, 206 [2](#)
- Kamata, K., & Nishimura, J. 1958, *Progress of Theoretical Physics Supplement*, 6, 93 [5](#)
- Knurenko, S. P., Kozlov, V. I., Petrov, Z. E., & Pravdin, M. I. 2013, *Journal of Physics Conference Series*, 409, 012070 [2](#)
- Ludwig, M., & Huege, T. 2011, *Astroparticle Physics*, 34, 438 [2](#), [10](#)
- Marin, V. 2012, *ArXiv e-prints* [2](#)
- Marin, V., & Revenu, B. 2012, *Astroparticle Physics*, 35, 733 [2](#), [3](#), [10](#)
- Martineau-Huynh, O., Ardouin, D., Cârloganu, C., et al. 2012, *Nuclear Instruments and Methods in Physics Research A*, 662, 29 [2](#)
- Melrose, D., & McPhedran, R. 2005, *Electromagnetic Processes in Dispersive Media* (Cambridge University Press) [2](#)
- Nigl, A., Apel, W. D., Arteaga, J. C., et al. 2008, *A&A*, 488, 807 [10](#)
- Roh, S., Kim, J., Ryu, D., et al. 2013, *ArXiv e-prints* [4](#)
- Scholten, O., Werner, K., & Rusydi, F. 2008, *Astroparticle Physics*, 29, 94 [2](#)
- Schoorlemmer, H., & Pierre Auger Collaboration 2012, *Nuclear Instruments and Methods in Physics Research A*, 662, 134 [2](#)
- Schröder, F. G., Apel, W. D., Arteaga-Velázquez, J. C., et al. 2013, in *American Institute of Physics Conference Series*, *American Institute of Physics Conference Series*, vol. 1535, edited by R. Lahmann, T. Eberl, K. Graf, C. James, T. Huege, T. Karg, & R. Nahnauer, 78–83 [1](#)
- Sciutto, S. J. 1999, *ArXiv Astrophysics e-prints* [4](#)
- Werner, K., de Vries, K. D., & Scholten, O. 2012, *Astroparticle Physics*, 37, 5 [2](#)
- Werner, K., & Scholten, O. 2008, *Astroparticle Physics*, 29, 393 [2](#), [10](#)